January 15, 2003

# Radio and Hard X–ray Images of High–Energy Electrons in a Compact X-class Solar Flare

S. M. White[1], S. Krucker[2], K. Shibasaki[3], T. Yokoyama[3], M. Shimojo[3] and M. R. Kundu[1]

[1]*Astronomy Department, University of Maryland, College Park, MD 20742*

[2]*Space Sciences Laboratory, University of California, Berkeley CA 94720-7450*

[3]*Nobeyama Radio Observatory, NAO, Minamisaku, Nagano 384-13, Japan*

white@astro.umd.edu

## ABSTRACT

We present the first comparison between radio images of high–energy electrons accelerated by a solar flare and images of hard X–rays produced by the same electrons at photon energies above 100 keV. The radio and hard X–ray light curves match each other well and both light curves and spectra are quantitatively consistent with an origin in a single population of nonthermal electrons with a power law index of around 4.5–5. The images indicate that the radio emission comes from an arcade of loops, with hard X–rays from their footpoints. Radio brightness temperatures exceed $10^9$ K and the peak in the radio spectrum is as high as 30 GHz: both these features point to very high densities of nonthermal electrons, possibly as high as $10^{11}$ cm$^{-3}$ above 10 keV at the peak of the flare.

*Subject headings:* Sun: flares – Sun: corona – Sun: radio radiation

## 1. INTRODUCTION

The launch of the Ramaty High Energy Solar Spectroscopic Imager (RHESSI), with its ability to image flares in hard X–rays and $\gamma$–rays at arcsecond resolution, offers us the opportunity to compare the emissions from electrons in the same energy range at two very different wavelength regimes: hard X–rays (bremsstrahlung) and radio (gyrosynchrotron). Both of these emissions are produced by nonthermal electrons with energies in excess of 100 keV, yet the emission mechanisms have very different properties and offer information on different aspects of conditions in the corona.

Bremsstrahlung is produced by collisions and therefore requires high densities: in most cases hard X–rays above 100 keV arise from nonthermal electrons striking the chromosphere and images show us the footpoints of the coronal loops carrying the accelerated electrons. Gyrosynchrotron emission is produced when electrons are accelerated by their gyromotion in coronal magnetic fields. This mechanism is extremely efficient and allows us to detect electrons with energies of hundreds of keV even in very small flares. On the other hand, flares in which X–rays above 100 keV can be imaged are rare because the steeply falling power law spectra do not yield sufficient photons at high energies for image formation.

Most previous comparisons of hard X–ray and radio images involve hard X–rays below 50 keV whose source is dominated by electrons with energies much lower than those that typically produce the nonthermal radio emission. Frequently it is found that the two populations of nonthermal electrons seem to have different energy spectra, implying that they have different origins (e.g., Kundu et al. 1994; Silva et al. 2000). Early comparisons of radio and hard X–ray images were carried out by Hoyng et al. (1983) and Kundu (1984). The largest study comparing radio and hard X–ray images of flares has been carried out by Nishio et al. (1997) and Nishio et al. (2000) who analyzed radio and hard X–ray emission from 25 flares. In most cases the hard X–rays seem to come from loop footpoints. In a number of cases the microwave sources also appear at one or more footpoints or legs of loops, and in other cases they come from the whole coronal loop. Other recent studies confirm this overall result (e.g., Takakura et al. 1994; Kundu et al. 1995; Gopalswamy et al. 1995; Hanaoka 1999; Kundu et al. 2001).

The excellent RHESSI data for the 2002 July 23 X4.5 flare allow us to make images at hard X-ray energies above 100 keV and compare these with simultaneous radio images of the nonthermal electrons at energies that produce the high energy photons. Radio images of this event from the Nobeyama Radio Heliograph (NoRH) have a spatial resolution and temporal cadence that are well matched to the RHESSI data and provide a complementary view of the electrons accelerated by this flare.

## 2. THE OBSERVATIONS

### 2.1. Data sources

NoRH observes the Sun at 17 and 34 GHz. The cleaned radio images are restored with beams of $10''$ at 17 GHz and $8''$ at 34 GHz. We compare these data with 12–20 keV and 100–150 keV hard X–ray images from RHESSI(made using grids 3 to 8 and reconstructed with $7''$ resolution), and with 195 Å images from the Transition Region and Coronal Explorer (TRACE) satellite. The 12–20 keV hard X–rays should be dominated by the hot thermal plasma component, while the

100–150 keV hard X–rays should be dominated by bremsstrahlung from the nonthermal electrons with energies over 300 keV. The 195 Å passband of TRACE is dominated by an Fe XII line formed at 1–2 $\times$ $10^6$ K, but also contains an Fe XXIV line at 192.03 Å (formed at 10-20 $\times$ $10^6$ K) that is usually much weaker (Handy et al. 1999).

Spatial coalignment of images at different wavelengths requires care. The NoRH data have an intrinsic uncertainty of order $10''$ and the self–calibration steps applied to the radio data to improve the images can introduce further uncertainty. Prior to the main impulsive phase we coalign the radio images using high density structures that show up in both radio and EUV images. During the impulsive phase we use a feature common to the radio, EUV and X–ray images as described below. The RHESSI solar image positions calculated by the pointing software were assumed to be correct, and this is confirmed by the overlays discussed below.

### 2.2. Time profiles

The radio and hard X–ray time profiles of the event are compared in Figure 1. The radio data is 35 GHz polarimeter data from Nobeyama Radio Observatory, which we compare with the 60–100 keV hard X–ray light curve from RHESSI (pile–up is not a problem in this energy range, unlike lower energies). The structure of the 35 GHz light curve is representative of all radio frequencies above 4 GHz, and 60–100 keV is representative of the light curves for all hard X–rays above 30 keV; below 30 keV the X–rays show less temporal fine structure in their light curves (Holman et al. 2003).

The main impulsive phase begins at 00:27:25, but the first sign of an increase in radio emission is at 00:22, when the soft X–rays ($<$ 10 keV) also begin to rise. Harder X–rays ($>$ 40 keV) don't start to rise until 00:26 UT, when the radio emission also shows a step increase. The impulsive phase consists of a number of spikes and dips that are all seen in both the radio and hard X–ray light curves. Different peaks have relatively different heights at the two wavelengths, but over the $\approx$ 20 minutes of the impulsive phase the similarity in time profiles is striking, including the brief sharp dip at 00:30:20.

Radio fluxes as a function of time at the frequencies 1.0, 2.0, 3.8, 9.4, 17, 35 and 80 GHz are available from the polarimeter patrol telescopes at Nobeyama. The lower panel in Fig. 1 represents the spectral evolution of the radio emission using two parameters: the peak frequency, and the radio spectral index from 35 to 80 GHz. The peak frequency in the spectrum, i.e., the frequency at which the radio flux is largest at any time, represents the boundary between optically thick low frequency emission and optically thin high frequency emission. The peak frequency shown in Fig. 1 is determined by fitting a parabola to the logarithm of the flux values at the three frequencies

closest to the peak. This is equivalent to fitting a gaussian function to the data near the peak. Staehli et al. (1989) fit radio spectra with a 4–parameter function that represents the theoretical spectral shape, but their function does not fit the spectra observed in this event, having a peak that is too sharp for the observed spectra. The peak frequency obtained from our fits is not very accurate (the coarse frequency resolution of the data makes it hard to estimate uncertainties), but trends in the peak frequency should be correct.

Away from the impulsive phase, the peak frequency determined in this way is usually close to 10 GHz because of a fairly constant ratio of the 17 GHz flux to the 9.4 GHz flux, but between 00:27:30 and 00:33:00, the peak frequency is well above 10 GHz, reaching 30 GHz at the onset of the impulsive phase and after the large dip at 00:30:20. This is a very large value for the peak frequency, which more typically is 7–10 GHz for solar radio bursts (Guidice & Castelli 1975; Staehli et al. 1989, 1990, however see also Ramaty et al. 1994). Further, it is unusual for the peak frequency to change during a given event by such a large amount as it does here (e.g., see the discussion by Belkora 1997). Since we can assume that the magnetic field strength in the radio source probably does not increase dramatically with time as the source expands, the increase in the peak frequency to such high values in this event is an indicator of very high densities of nonthermal electrons in the radio source (Staehli et al. 1989; Ramaty et al. 1994), as we discuss further in section 4.

The high–frequency spectral index of an optically thin gyrosynchrotron radio source can be used to infer the energy distribution of the radiating electrons. The radio spectral index $\alpha$ found here lies consistently between $-3$ and $-4$, showing little correlation with peak frequency, so we regard this value as reliable. We adopt the Dulk & Marsh (1982) gyrosynchrotron approximation $\alpha \approx 1.22 - 0.90\delta$ to convert $\alpha$ into an electron energy power law index $\delta$ ($n(E) \propto E^{-\delta}$), and find $\delta = 3.7$ to 4.8. When the peak frequency is very high, the 35 to 80 GHz slope is flatter than the true optically thin slope and $\delta$ will be underestimated by this calculation.

## 3. SOURCE MORPHOLOGY

### 3.1. Preflare

Preflare conditions are shown in panels (a,b) of Figure 2. While the EUV image shows nothing remarkable, the radio image is quite extraordinary. For at least an hour prior to the flare, back to 23 UT (dawn at NoRH), an elongated loop structure is visible in both the 17 and 34 GHz images. The loop extends over $80''$ to the north-east. In the 75 minutes prior to the flare the loop does not seem to change shape, nor are there significant changes in brightness. There is one important difference between the 17 and 34 GHz images: the 17 GHz images show a bright compact source at the

base of the loop that has no counterpart at 34 GHz, or in the EUV. The peak 17 GHz brightness temperature in this source declines steadily from $7 \times 10^5$ K at 23 UT to $2.5 \times 10^5$ K at 00:15 UT. The loop has a radio spectrum consistent with optically thin thermal radio emission (brightness temperatures of 100–120 $\times$ $10^3$ K at 17 GHz and about 1/4 as much at 34 GHz). This loop could be a hot post-flare loop from an earlier event: if so, it must be at a temperature well above the formation temperature of Fe XII, $\approx 1.5 \times 10^6$ K, and it is interesting that the EUV images show no signs of plasma from this hot loop cooling into the Fe XII range.

The compact 17 GHz peak is undetected in the 34 GHz image and the 17 to 34 GHz ratio is in excess of 6 for this feature and requires a nonthermal emission mechanism. This is essentially the location where the flare starts.

### 3.2. Flare onset

Panels (c) and (d) of Fig. 2 show images during flare onset, with important features in the TRACE 195 Å image (panel d) labelled in both panels. The TRACE images in panel (d) and subsequent TRACE panels show a $64''$ field of view in order to emphasize structure within the compact flare site better, while the radio images in the left column of panels continue to be $128''$ across. The linear features in the TRACE image (d) labelled "ribbons" appear to be very low in the atmosphere. The right-hand ribbon is the first flare feature to appear in the 195 Å images, at 00:21:29. The NoRH images show emission starting at 00:21:00 UT, with a faint sign of emission from the ribbon, but with the strongest emission extending from the location of the brightest 17 GHz feature in panel (a) northwards for about $20''$. By 00:22:00 UT, the peak 17 GHz brightness temperature in the right hand ribbon is of order $10^5$ K, while it is $10^6$ K in the brightest radio source. Both these features should be detected at 34 GHz at this time if the radio emission is due to thermal bremsstrahlung, but the images show no emission. We conclude that the radio emission is nonthermal, and that acceleration to energies of hundreds of keV commenced at 00:21:00 UT even though there is no indication of bremsstrahlung from these electrons in the 60–100 keV light curve at this time.

At the time shown in panels (c,d), 00:24:57, the ribbon is clearly visible in the TRACE 195 Å image (panel d), the 17 (contours in panel c) and 34 (inset in panel c) GHz radio images and the RHESSI 12–20 keV image (greyscale in panel c), allowing coalignment of the different wavelengths to within several arcseconds at this time. In addition to the western ribbon, the 195 Å image at this time shows a ribbon to the east (arrowed), also low in the atmosphere, as well as what seems to be a high diffuse loop connecting the eastern and western sides of the flare region (arrowed). Inspection of the sequence of 195 Å images leading up to this time indicates that the pattern of brightening at this wavelength is actually quite complex, with a mixture of sharp linear

features apparently low in the atmosphere and curved, more diffuse features higher in the corona. From the coincidence of the 34 GHz, 12–20 keV and 195 Å images of the bright loop at 00:24:56 and its diffuse appearance, we argue that the TRACE image does not show Fe XII but rather Fe XXIV emission from within the TRACE 195 Å passband. Fe XXIV has a formation temperature of order 10–20 $\times$ $10^6$ K, so this loop feature is the first sign of hot soft X–ray emitting plasma. It is brightest at its eastern end in both 12–20 keV hard X-rays and at 34 GHz, as would be expected due to projection effects in a high east–west loop near the limb. From the difference between the 17 and 34 GHz images, we argue that 17 GHz is dominated by steep spectrum nonthermal electrons while the 34 GHz emission is thermal bremsstrahlung from the soft X–ray loop.

### 3.3. Flare development

The 100–150 keV hard X-rays are not strong enough to be imaged until 00:27:45, when they show two compact sources of similar strength separated by about 12″ along a SE–NW direction (panel e). They are located to the west of the 12–20 keV hard X–ray peak, which still resembles the 195 Å image. The radio source remains fairly compact, but the 17 GHz peak brightness temperature has jumped from 6.0 $\times$ $10^6$ K at 00:24:57 to 8.5 $\times$ $10^8$ K. From this time on the TRACE 195 Å images are saturated, but are consistent with an arcade of loops seen in projection close to the limb. Only the westernmost loops in the arcade have footpoints lying on the first ribbon to brighten, while the eastern footpoints are obscured by the loop tops. As time proceeds the arcade lengthens to the north–east, and the original loops at the western end of the arcade tend to fade. The RHESSI 12–20 keV images are consistent with thermal plasma near the tops of these loops, while the 100–150 keV images continue to show a pair of sources whose separation increases with time, and the axis joining the two sources appears to rotate gradually anticlockwise with time (Krucker et al. 2003).

Overall, the 17 GHz radio source does not change its size or morphology greatly from 00:27 to 00:40. Spatially, the peak of the radio emission appears to lie at the top of the arcade of loops seen in the 195 Å images, close to the peak in the 12–20 keV hard X–ray images. The peak brightness temperature in the 17 GHz images reaches $10^9$ K at 00:28:00 UT and peaks at 1.4 $\times$ $10^9$ K at 00:31:00, after the sharp dip in flux. At this time 17 GHz is on the optically thick side of the spectral peak, so the brightness temperature should represent the mean energy of the electrons contributing most to the 17 GHz flux: 1.4 $\times$ $10^9$ K corresponds to a kinetic energy of order 120 keV. In fact, gyrosynchrotron emission has a broad energy response and this mean energy represents the contribution of a wide range of energies. Since the value of 1.4 $\times$ $10^9$ K is averaged over a gaussian beam of 10″ it is possible that even higher brightness temperatures would be measured at higher spatial resolution. The high brightness temperature of the radio emission is responsible for the

very high radio fluxes observed in this event (200 times the quiet–Sun flux at 17 GHz) despite its small spatial size.

Fig. 2 shows where the peak circular polarization lies in the 17 GHz images. The polarization in this flare is relatively weak, being 1–2% early in the impulsive phase, increasing to 5–10% later, but the images consistently show right circular polarization from the vicinity of the footpoints on the western side of the arcade and left circular polarization from the eastern side of the arcade. The low degree of polarization is consistent with the fact that the flare is close to the limb (much of the source may be viewed nearly orthogonal to the magnetic field), and 17 GHz is below the spectral peak, and hence optically thick, for much of the time.

## 4. DISCUSSION

### 4.1. Electron energy distribution

As noted above, the high frequency radio spectral index implies a power law electron energy distribution with an index of $\delta \approx 3.7$–$4.8$. We have fit the RHESSI hard X–ray spectrum from 40 to 400 keV with a broken power law using the SPEX program and find that from 00:28:00 to 00:37:00, the spectrum above 100 keV has a constant slope between -2.9 and -3.1 (see also Holman et al. 2003). Assuming that the slope of -3 represents thick target emission, the corresponding electron energy spectrum has a power–law slope of $\delta \approx 4.5$. The value of $\delta$ inferred from the radio data at this time is consistent with this value.

If the spectral indices of the radio–emitting and hard X–ray–emitting electrons are the same, we can compare the number densities of electrons required at the two wavelength ranges. We follow the procedure outlined by Nitta et al. (1991). We choose the time around 00:35:00 when the radio spectral peak is well below 34 GHz and hence the 34 GHz emission is optically thin. The photon energy ($E_\gamma$) spectrum at this time has the form $9\,(E_\gamma/50\,\mathrm{keV})^{-3.24}$. The corresponding flux of electrons striking the chromosphere to produce the observed hard X–ray flux is $3 \times 10^{35} E^{-4.24}$ electrons (keV s)$^{-1}$ (Hudson et al. 1978). To convert this to a number density we need to divide by the footpoint area $A$. The RHESSI images do not resolve the footpoints at a resolution of $7''$ and images made using grid 1 suggest a size as small as $2''$. We adopt $A = 10^{17}$ cm$^2$ and assume electron energy equipartition between the three directions of motion, leading to an energy distribution for the electron density at the footpoints of $8 \times 10^{14}\, E_{\mathrm{keV}}^{-4.74}$ electrons cm$^{-3}$ keV$^{-1}$. At this time the radio spectral index is $-3.4$, consistent with an energy spectral index of $-4.74$ to within the uncertainties, and the 34 GHz peak brightness temperature is $1.8 \times 10^8$ K. Using the approximate gyrosynchrotron formulae from Dulk & Marsh (1982) and Dulk (1985) with a line–of–sight depth through the source of $5 \times 10^8$ cm and an angle between the magnetic field and the

line of sight of $\sin^{-1}(0.8)$, we find the electron energy density distribution from the radio data to be $8 \times 10^{15}\ (B/500\,\mathrm{G})^{-4.07}\ E_{\mathrm{keV}}^{-4.74}$ electrons cm$^{-3}$ keV$^{-1}$. Given the strong dependence on $B$ and the uncertainty in $A$ and in the Dulk & Marsh (1982) approximations to the exact gyrosynchrotron emissivity, we regard the hypothesis that these two densities are consistent with one another for plausible $B$ and $A$ as being likely to be true. Despite the discrepancy between the radio images and the 100–150 keV hard X–ray images, the nonthermal radio and hard X–ray emission appear to come from the same electron population. Note that these expressions imply extremely high number densities for nonthermal electrons. If the electron energy spectrum continues down to 10 keV, the energy–integrated number density of nonthermal electrons at this time is $8 \times 10^9$ cm$^{-3}$, and the energy density associated with these electrons is of order 160 ergs cm$^{-3}$.

### 4.2. Morphological changes

An obvious issue to be addressed is whether the peaks in the light curves in Fig. 1 are associated with major changes in the spatial morphology of the source. Inspection of the sequence of 100–150 keV hard X–ray images does reveal an interesting trend: the images at the subsidiary peaks at 00:28:50, 00:29:30, 00:30:50, and 00:35:10 all differ from the images at the immediately preceding dips by showing markedly increased emission at the southern source. However, in the later peak at 00:38:35 the hard X-ray emission shows a larger increase at the northern source. Krucker et al. (2003) present light curves for the different hard X–ray sources.

To compare this behaviour with the radio emission, Figure 3 shows two examples of the changes in morphology: the sudden dip at 00:30:20 (upper panels), and the later peak just after 00:38:00 UT (lower panels). The dramatic sudden dip at 00:30:20 is seen in both hard X–rays (above but not below 20 keV) and in the radio light curves. Fig. 3a shows that during the dip the radio emission is dominated by an elongated source along the tops of the arcade of loops in the 195 Å image (Fig. 1h). At 34 GHz emission to the south is also seen. After the rise in emission, the additional 34 GHz emission takes the form of the legs of a loop oriented north–south, while the 17 GHz emission is dominated by bright emission where the top of this loop would be. The hard X–ray difference image shows that the brightest new flux comes from the southern source, while the 34 GHz radio emission is more symmetric. Note that the relative position of the hard X–ray and radio sources is uncertain by up to $10''$. At this time 17 GHz is well below the peak frequency: if a loop with $B$ stronger at the footpoints than at the loop top is viewed from the side one expects the optically thick 17 GHz emission to be brightest at the loop top (where $B$ is weaker) and the optically thin 34 GHz emission to be brightest at the footpoints where $B$ is stronger, as appears to be the case here.

In the second example, the hard X–rays show a larger increase in the northern source dur-

ing the peak. Again, the increase in radio emission is fairly symmetric between the northern and southern sources, showing a morphology with two elongated, oppositely circularly polarized sources roughly aligned with the arcade footpoints. This morphology is maintained for the next 10 minutes.

## 5. CONCLUSIONS

Observations of the 2002 July 23 event are consistent with the general picture of nonthermal electrons at energies of many hundreds of keV radiating at radio wavelengths as they travel along the coronal portion of the loop and 100–150 keV hard X–rays when they strike the chromosphere at the footpoints of magnetic field lines. A single population of electrons with a power–law index of about $-4.5$ to $-5$ above 100 keV can produce the emission at both wavelengths: the radio and hard X–ray light curves show essentially identical structure with many individual peaks. This is in contrast to many other events in which the radio and hard X–rays seem to be from different nonthermal populations. One of the reasons for the large radio flux from this spatially relatively compact event lies in the high brightness temperatures: we measure at least $1.4 \times 10^9$ K, one of the highest measurements ever for incoherent emission from a solar flare. The peak frequency in the radio spectrum also achieves very high values of up to 30 GHz, requiring very high densities of nonthermal electrons: at least $10^{10}$ electrons cm$^{-3}$ above 10 keV are required at the peak of the event, implying an acceleration mechanism of very high efficiency.

Prior to the flare the radio images show a highly distended loop, rooted in the eventual flare site, that is not visible at other wavelengths investigated. The flare starts with ribbons low in the atmosphere that are visible at radio, X–ray and EUV wavelengths, and expands to fill an arcade of magnetic field lines with nonthermal particles. The light curve contains peaks with separations of order minutes that require separate injections of nonthermal electrons. Difference radio images show symmetric distributions of emission produced by these injections.

The data for this event provide a challenge for our understanding of flares. A single electron energy population with a power law spectrum of $\delta = 4.74$ can explain both radio and hard X–ray data, but calculations show that brightness temperatures over $10^9$ K can only be achieved by such a steep spectrum at harmonic numbers over 30 (see figures in Dulk & Marsh 1982, confirmed by our own calculations), implying a magnetic field no more than 200 G. To compensate for the lower value of $B$, nonthermal densities over $10^{11}$ cm$^{-3}$ above 10 keV are required, and such high nonthermal densities are not usually regarded as plausible. The RHESSI data do not constrain the lower energy cutoff in the nonthermal spectrum due to masking by the strong thermal emission that prevents detection of the footpoints below 20 keV (Krucker et al. 2003), but even above 20 keV nonthermal densities over $10^{10}$ cm$^{-3}$ are required.

This research was supported by NSF grants ATM 99-90809 and INT-98-19917, and NASA grants NAG 5-8192 and NAG 5-10175. We gratefully acknowledge the open-data policies of NoRH, the NASA satellite TRACE and the ESA/NASA satellite SOHO and their instrument teams which make multi-wavelength research such as this much easier.

## REFERENCES

Belkora, L. 1997, Astrophys. J., 481, 532

Dulk, G. A. 1985, Ann. Rev. Astron. Astrophys., 23, 169

Dulk, G. A. & Marsh, K. A. 1982, Astrophys. J., 259, 350

Gopalswamy, N., Raulin, J. P., Kundu, M., Nitta, N., Lemen, J. R., Herrmann, R., Zarro, D., & Kosugi, T. 1995, Astrophys. J., 455, 715

Guidice, D. A. & Castelli, J. P. 1975, Solar Phys., 44, 155

Hanaoka, Y. 1999, Publ. Astron. Soc. Japan, 51, 483

Handy, B. N., Acton, L. W., Kankelborg, C. C., et al. 1999, Solar Phys., 187, 229

Holman, G. D., Sui, L., Schwartz, R. A., & Emslie, A. G. 2003, Astrophys. J. (Lett.), submitted

Hoyng, P., Marsh, K. A., Zirin, H., & Dennis, B. R. 1983, Astrophys. J., 268, 865

Hudson, H. S., Canfield, R. C., & Kane, S. R. 1978, Solar Phys., 60, 137

Krucker, S., Hurford, G. J., & Lin, R. P. 2003, Astrophys. J. (Lett.), submitted

Kundu, M. R. 1984, Adv. Space Res., 4, 157

Kundu, M. R., Nindos, A., White, S. M., & Grechnev, V. V. 2001, Astrophys. J., 557, 880

Kundu, M. R., Nitta, N., White, S. M., Shibasaki, K., Enome, S., Sakao, T., Kosugi, T., & Sakurai, T. 1995, Astrophys. J., 454, 522

Kundu, M. R., White, S. M., Gopalswamy, N., & Lim, J. 1994, Astrophys. J. Supp., 90, 599

Nishio, M., Kosugi, T., Yaji, K., Nakajima, H., & Sakurai, T. 2000, Advances in Space Research, 25, 1791

Nishio, M., Yaji, K., Kosugi, T., Nakajima, H., & Sakurai, T. 1997, Astrophys. J., 489, 976

Nitta, N., White, S. M., Kundu, M. R., Gopalswamy, N., Holman, G. D., Brosius, J. W., Schmelz, J. T., Saba, J. L. R., & Strong, K. T. 1991, Astrophys. J., 374, 374

Ramaty, R., Schwartz, R. A., Enome, S., & Nakajima, H. 1994, Astrophys. J., 436, 941

Silva, A. V. R., Wang, H., & Gary, D. E. 2000, Astrophys. J., 545, 1116

Staehli, M., Gary, D. E., & Hurford, G. J. 1989, Solar Phys., 120, 351

—. 1990, Solar Phys., 125, 343

Takakura, T., Nishio, M., Nakajima, H., Enome, S., Shibasaki, K., Takano, T., Hanaoka, Y., Kosugi, T., Sakao, T., Masuda, S., Makashima, K., & Inda-Koide, M. 1994, Publ. Astron. Soc. Japan, 46, 653

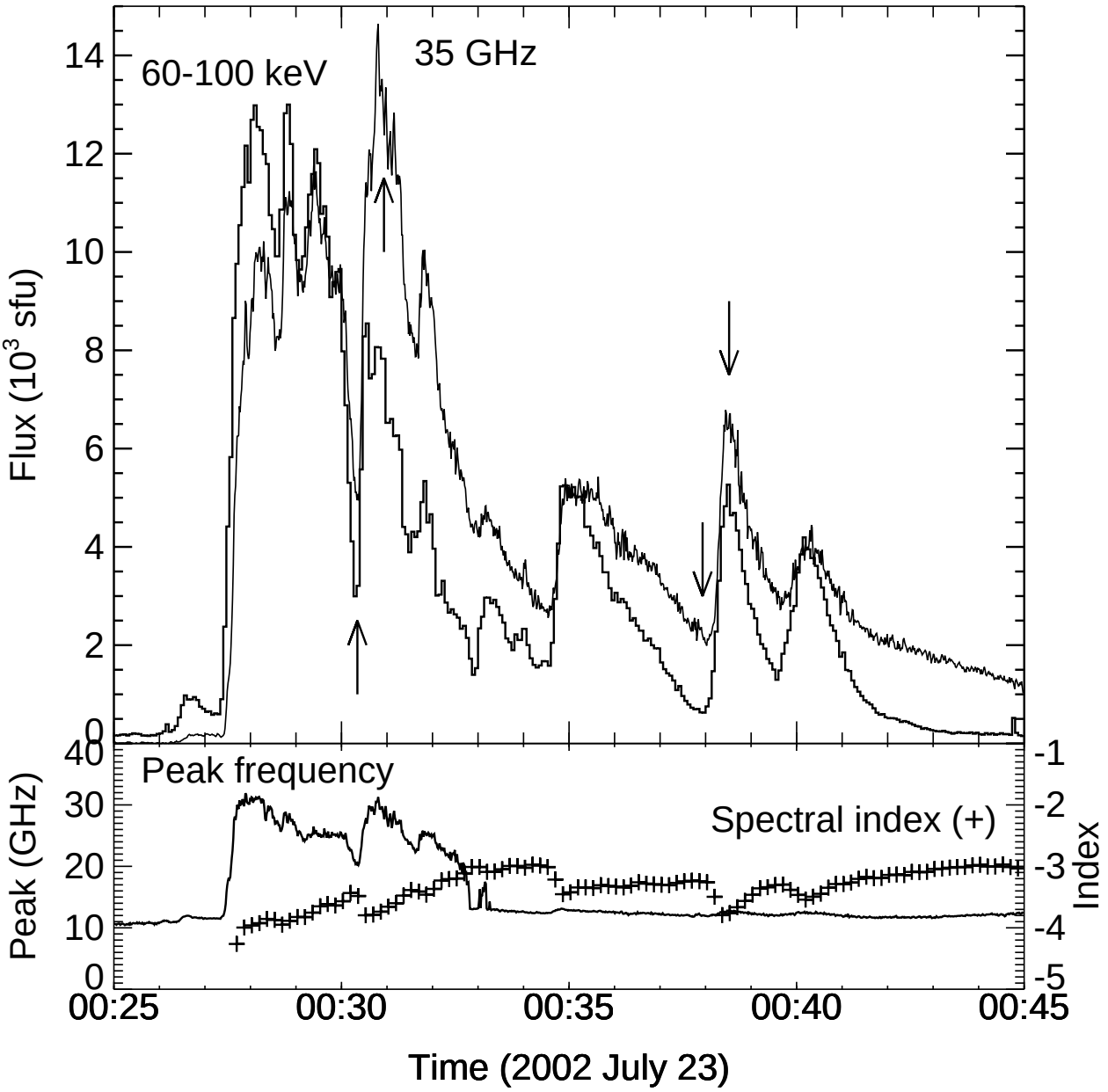


Fig. 1.— Comparison (upper panel) of the RHESSI 60–100 keV hard X-ray light curve (histogram) and the Nobeyama Radio Observatory 35 GHz polarimeter light curve (solid curve) for the 2002 July 23 flare, as well as (lower panel) the time evolution of the radio spectral peak frequency (line) and the spectral index from 35 to 80 GHz (plus symbols). Arrows indicate the times of images shown in Figure 3.

Fig. 2.— Images of the flare at X-ray, EUV and radio wavelengths. The top row of panels shows radio and EUV images in the preflare phase. On the left are 17 GHz contours overlaid on a greyscale 34 GHz image (both averaged over the period 23:00–00:15 UT), while the right panel shows the TRACE 195 Å image from 00:18:19 UT, dominated by the Fe XII line, together with two 17 GHz contours for context. The remaining rows of panels have a common format: on the left a $128'' \times 128''$ RHESSI greyscale image of 12–20 keV hard X–rays is overlaid with 17 GHz total intensity radio contours (solid) and RHESSI 100–150 keV hard X–ray contours (dashed), while on the right a $64'' \times 64''$ TRACE 195 Å image of the region outlined by a white dashed border in panel (b) is overlaid with solid grey contours showing the RHESSI 12–20 keV hard X–rays and dashed black contours showing the RHESSI 100–150 keV hard X–rays (as in the left panel). Panels (f,h,j,l) also contain white contours showing the right (solid) and left (dashed) circularly polarized 17 GHz emission at 80% of the respective maxima. The panel labels refer to the times of the 17 GHz images (left) and the TRACE images (right). Panel (c) also contains an inset showing the 34 GHz image at 00:24:58, on the same scale as the rest of the panel, as well as labels for important features of the 195 Å image. The arrows are reproduced in panel (d). Contours for the 17 GHz and 12–20 keV images are at powers of $e$ times 4 $\times$ the noise level in the respective images. The 100–150 keV contours are at 3,5,7,9,... times the noise level. The 17 GHz restoring beam size of $10''$ is shown in panel (k); in panel (c) the preflare 17 GHz image (panel a) has been subtracted from the image shown in contours to emphasize the changes.

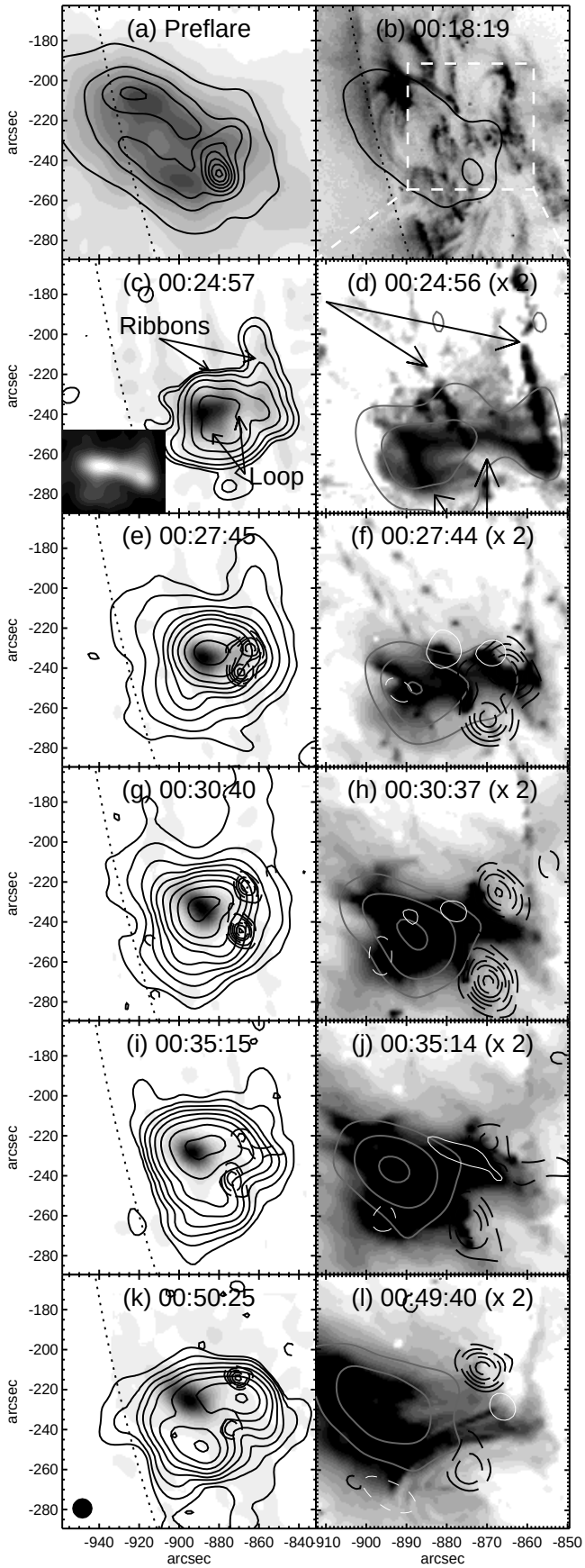
(a) Preflare
(b) 00:18:19
(c) 00:24:57
Ribbons
Loop
(d) 00:24:56 (x 2)
(e) 00:27:45
(f) 00:27:44 (x 2)
(g) 00:30:40
(h) 00:30:37 (x 2)
(i) 00:35:15
(j) 00:35:14 (x 2)
(k) 00:50:25
(l) 00:49:40 (x 2)
arcsec
-180
-200
-220
-240
-260
-280
-940 -920 -900 -880 -860 -840
-910 -900 -890 -880 -870 -860 -850

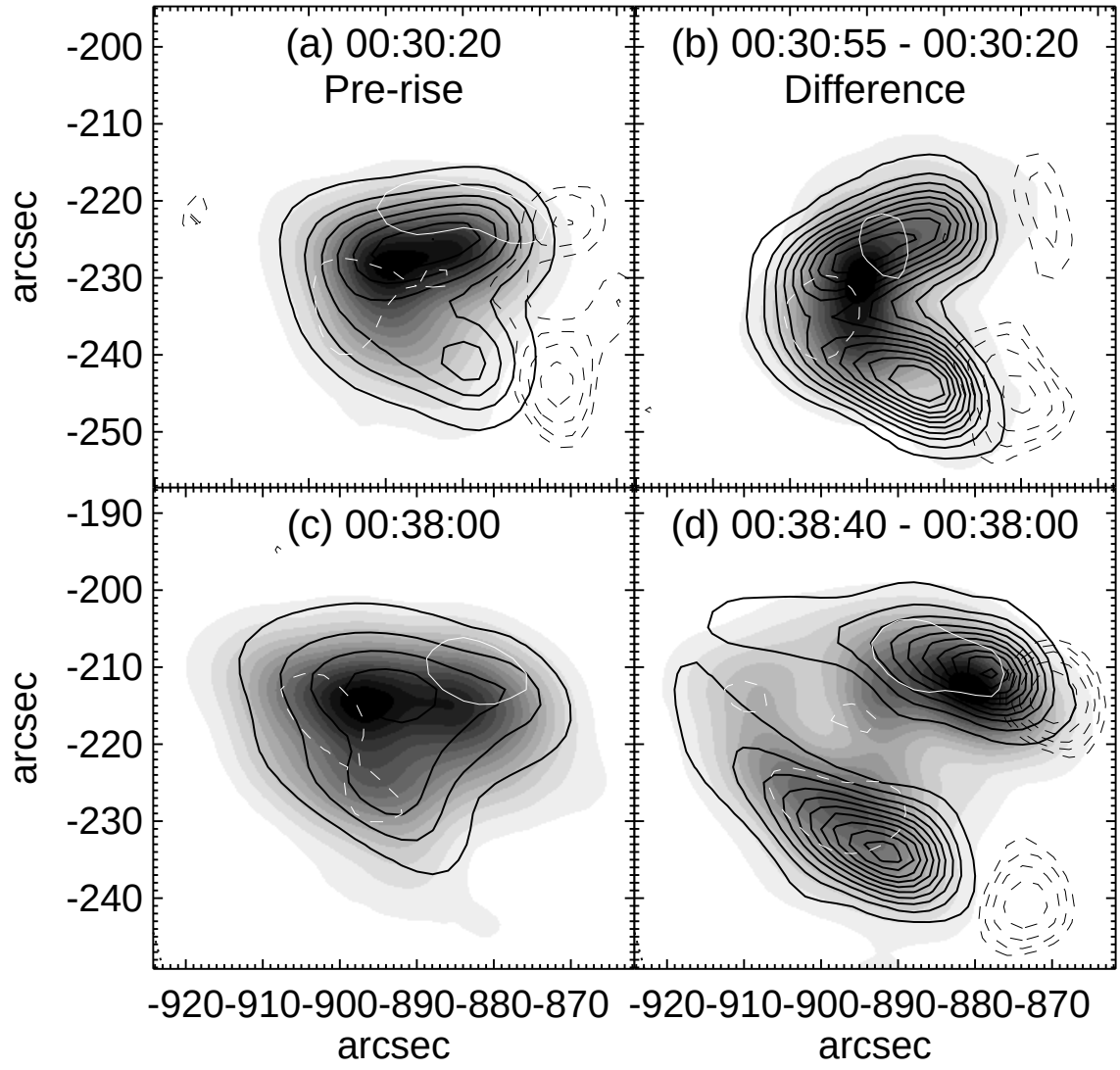


Fig. 3.— Comparison of the radio images before and after two jumps in the radio flux: after the sharp dip at 00:30:20 (upper panels), and after the secondary peak starting at 00:38:00 (lower panels). The greyscale image and the black contours in the left panels show the 17 and 34 GHz images, respectively, while in the right panels they show the difference images (image at later time shown in label minus image at earlier time). The 34 GHz contours are at 5,15,...,95% of the maximum 34 GHz flux in the right panel ($2.5 \times 10^8$ K in panels a,b; $1.4 \times 10^8$ K in panels c,d). The white contours are the 60% levels of circular polarization at 17 GHz at the times labelled (not difference images in panels b,d), while the dashed black contours indicate the location of the simultaneous 100–150 keV hard X–ray emission (raw image on left, difference image on right).